Ultrahigh-Resolution Wireless Capacitance Readout Based on a Single Real Mode in a Perturbed *PT*-Symmetric Electronic Trimer Sandwich

Ke Yin, Yuangen Huang, Wenjing Yin, Xianglin Hao, Xikui Ma, and Tianyu Dong*
School of Electrical Engineering, Xi'an Jiaotong University, Xi'an 710049, China

(Received 7 September 2022; revised 3 October 2022; accepted 7 November 2022; published 7 December 2022)

High-performance interrogation of an inductor-capacitor microsensor has been a long-standing challenge due to the limited size of the sensor. Parity-time (*PT*) symmetry, an intriguing concept originated from quantum physics, has been utilized to improve the spectral resolution and sensitivity of the conventional readout circuit, while the *PT*-symmetry condition has to be satisfied. In this work, a sandwich-type wireless capacitance readout mechanism based on perturbed *PT*-symmetric electronic trimer without manual tuning of the reader circuit is proposed. Theoretical eigenvalue analysis by solving the system equations shows that the system exhibits single real mode in weak coupling regime whose eigenfrequency changes in response to the capacitance of the neutral resonator. Furthermore, the proposed readout system exhibits wider readout capacitance range compared to the standard *PT*-symmetry-based system while retaining higher *Q* factor compared to the conventional readout method, which has been validated with the experimental prototype based on printed circuit board. Our work not only enriches the underlying theory of non-Hermitian physics, but also shows potential applications in scenarios where longer interrogation distance is required, such as implanted medical devices, parameter detection in harsh environment, etc.

DOI: 10.1103/PhysRevApplied.18.064020

I. INTRODUCTION

Thanks to the capability of remote inquiry and the unnecessity of additional power supply, inductor-capacitor (*LC*) passive sensor has been utilized for implanted medical devices to monitor physiological parameters of patients, such as intraocular pressure (IOP) [1], blood flow [2], wound pressure [3], and for parameter detection in harsh environment, such as pressure [4], temperature [5], and liquid permittivity [6], etc. A conventional *LC* wireless sensing system typically consists of a readout antenna and an inductively coupled passive *RLC* microsensor whose resonance frequency change, in response to the quantities to be measured, is wirelessly interrogated through the dip frequency shift of the reflection spectrum [7]. However, due to the large equivalent resistance caused by skin effect and eddy current loss, the real-life application of a *LC* microsensor has been limited by the low quality (*Q*) factor and poor resolution of the readout reflection spectrum. Great efforts have been made to design a sensing system with high *Q* factor, such as multiple spoof plasmon induced transparency with high *Q* group delays for surface-sensing applications [8] and AlN/sapphire-based surface acoustic wave resonators with high *Q* factors for high-temperature applications [9], etc. Moreover, the small size of microsensor results in weak coupling between the readout and the sensor coils, which further degrades the readout performance. In order to improve the readability and robustness of detection, the measured reflection dip should generally be sharp and narrow band.

Aiming to the above issue, parity-time (*PT*) symmetry has provided a solution to greatly enhance the *Q* factor of the reflection spectrum [10]. The concept of *PT* symmetry is presented in the context of quantum physics to describe a class of non-Hermitian Hamiltonians with real energy spectrum [11]. In recent years, such an appealing discovery has been fruitfully extended to other research areas, including photonics [12–14], electronics [10,15–26], microwaves [27,28], and acoustics [29–31]. Among them, non-Hermitian electronics has become an active research area, and opens up interesting avenues for applications, such as robust wireless power transmission (WPT) [17–20,32,33] and wireless microsensor readout with enhanced sensitivity and resolution [10,23–25].

This non-Hermitian *PT*-symmetry-enhanced wireless sensing system can typically work in two phases, viz., *PT*-symmetric phase and *PT*-broken phase. A standard second-order *PT*-symmetric telemetry system consists of two inductively coupled *RLC* resonators with balanced gain and loss, which has been utilized for interrogating resistive temperature sensors [24,34] and intracranial pressure sensors [25], etc. The second-order configuration can further be extended to the third-order system by incorporating three inductively coupled gain-neutral-loss *LC*

*tydong@mail.xjtu.edu.cn

resonators chain, in which a divergent exceptional point (DEP), i.e., $\kappa_D = 1/\sqrt{2}$, enables an infinity sensitivity in theory [23]. Therefore, by deliberately manipulating the system to work nearby DEP, i.e., $\kappa \approx 0.7$, the system can realize ultrasensitive wireless sensing. Nevertheless, such strong coupling has approached the upper limit of three linearly coupled inductors (see Appendix D for theoretical verification), which is not easy to realize in practical applications. Furthermore, these symmetry-phase-based readout systems require manual tuning of the reader circuit to satisfy the *PT*-symmetry condition and the coupling coefficient greater than κ_{EP} to guarantee the system operating in the *PT*-symmetric phase where high sensitivity and Q factor occurs.

Along different lines, it has been shown that the *PT*-symmetry breaking regime can enhance the remote interrogation distance while maintaining high Q factor [35]. However, cyclically scanning variable capacitance on the reader side utilized to track the change of the capacitive humidity sensor increases the system complexity and is time-consuming. Coupling-independent and real-time wireless resistive sensing system based on nonlinear *PT* symmetry has been reported to realize low-complexity readers [34]. Moreover, eigenfrequency evolution in response to the sensor-side capacitive perturbation when the system is biased at the exceptional point is investigated, showing that the eigenfrequency bifurcation follows a square-root-dependence on the capacitive perturbation parameter, which can be utilized to detect small signal changes [36]. Therefore, EP-enhanced capacitance readout can be utilized without the need of maintaining *PT* symmetry. In a later work, our group proposed a vector-network-analyzer-free *PT*-symmetric capacitance readout system with nonlinear gain in which the reader-side capacitance need not to be manually tuned [26]. However, in both these works [26,36], the readout sensitivity is not high and has yet to be extended to higher-order *PT*-symmetric systems, where greater sensitivity is envisioned.

In this work, we report a sandwich-type passive wireless capacitance readout system with ultrahigh Q factor based on perturbed *PT*-symmetric electronic trimer. We theoretically analyze the eigenfrequency evolution of the third-order *PT*-symmetric *LC* sensing system in response to the capacitive perturbation on neutral resonator, showing that single real mode can exist in the weak coupling regime. Furthermore, the proposed readout mechanism enables much sharper reflection dips and higher Q-factor capacitance readout compared to conventional *LC* sensors, and exhibits wider readout capacitance range compared to the standard second-order *PT*-symmetric system without the need of manually adjusting the capacitance on the gain (loss) side. Our work can enrich the underlying physics of non-Hermitian electronics and pave the way towards application scenarios where high-performance wireless readout with longer interrogation distance is required.

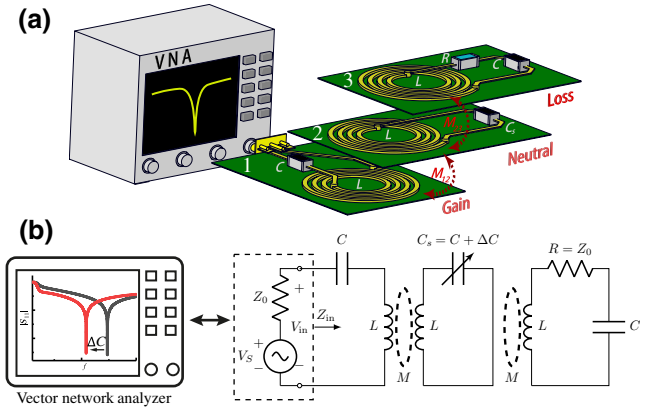

FIG. 1. (a) Illustration of a third-order parity-time symmetric wireless sensing system and (b) the corresponding circuit schematics.

II. THEORY: EIGENVALUE ANALYSIS OF PERTURBED *PT*-SYMMETRIC ELECTRONIC TRIMER

Figures 1(a) and 1(b) show the system illustration and the corresponding circuit schematics of the proposed wireless capacitance readout mechanism, respectively. The system is composed of an inductively coupled gain-neutral-loss *LC* resonator chain, which constitutes a *PT*-symmetric electronic trimer. Compared to the active *PT*-symmetric wireless sensing systems with negative resistance converter based on Colpitts-type circuit [24] or cross-coupled MOSFET pair [34], which requires extra power supply and increases the complexity of the reader, the gain element in our system is introduced by the vector network analyzer (VNA) for simplicity since the VNA itself is a radio-frequency source with characteristic impedance $Z_0 = 50\ \Omega$ and therefore can be treated as a $-50\ \Omega$ negative resistor. The loss is realized with a normal resistor whose resistance is deliberately chosen as $R = Z_0$ to guarantee balanced gain and loss, which is typically required in *PT*-symmetric systems. Different from standard third-order *PT*-symmetric systems where the capacitance of gain, neutral, and loss resonators are tuned together [23], we consider the case when only the neutral-side capacitance is changed, which is regarded as capacitive perturbation to the neutral resonator. Thus, no variation of the gain and loss side is needed to guarantee the parity symmetry as usual.

By defining a state vector $\Phi = (I_1, I_2, I_3, I_1', I_2', I_3')^T$ with $I_n (n = 1, 2, 3)$ denoting the inductor current on the gain, neutral and loss resonators, respectively, and $I_n' (n = 1, 2, 3)$ denoting their corresponding first-order derivatives with respect to the normalized time τ (see Appendix A for the detailed derivation), the system equation can be

expressed as

$$\frac{d\Phi}{d\tau} = \mathcal{L}\Phi, \tag{1}$$

where the Liouvillian $\mathcal{L}$ reads as

$$\mathcal{L} = \begin{pmatrix} 0 & 0 & 0 & 1 & 0 & 0 \\ 0 & 0 & 0 & 0 & 1 & 0 \\ 0 & 0 & 0 & 0 & 0 & 1 \\ -\frac{1-\kappa^2}{\tilde{\kappa}} & \frac{\kappa}{\eta\tilde{\kappa}} & -\frac{\kappa^2}{\tilde{\kappa}} & \gamma\frac{1-\kappa^2}{\tilde{\kappa}} & 0 & -\gamma\frac{\kappa^2}{\tilde{\kappa}} \\ \frac{\kappa}{\tilde{\kappa}} & -\frac{1}{\eta\tilde{\kappa}} & \frac{\kappa}{\tilde{\kappa}} & -\gamma\frac{\kappa}{\tilde{\kappa}} & 0 & \gamma\frac{\kappa}{\tilde{\kappa}} \\ -\frac{\kappa^2}{\tilde{\kappa}} & \frac{\kappa}{\eta\tilde{\kappa}} & -\frac{1-\kappa^2}{\tilde{\kappa}} & \gamma\frac{\kappa^2}{\tilde{\kappa}} & 0 & -\gamma\frac{1-\kappa^2}{\tilde{\kappa}} \end{pmatrix}. \tag{2}$$

Here, the parameter $\eta = C_s/C$ reflects the perturbation caused by the capacitive sensor; $\kappa = M/L$ is the mutual coupling coefficient and $\tilde{\kappa} = 1 - 2\kappa^2$; $\tau = \omega_0 t = t/\sqrt{LC}$ is the normalized time; $\gamma = Z_0\sqrt{C/L} = R\sqrt{C/L}$ is the normalized gain (loss) parameter. It is noted that the corresponding effective Hamiltonian $\mathcal{H}_{\text{eff}} = i\mathcal{L}$ is PT symmetric when $\eta = 1$. That is to say $\mathcal{H}_{\text{eff}}$ and PT are commutative, i.e., $[\mathcal{H}_{\text{eff}}, PT] = 0$, where the $\mathcal{P}$ and $\mathcal{T}$ operators, respectively, reads as

$$\mathcal{P} = \begin{pmatrix} \mathbf{J}_3 & 0 \\ 0 & \mathbf{J}_3 \end{pmatrix}, \tag{3a}$$

$$\mathcal{T} = \begin{pmatrix} \mathbf{I}_3 & 0 \\ 0 & \mathbf{I}_3 \end{pmatrix}\mathscr{K}, \tag{3b}$$

with $\mathbf{J}_n$ being an $n \times n$ exchange matrix ($J_{ij} = 1$ when $i + j = n + 1$ and $J_{ij} = 0$ when $i + j \neq n + 1$), $\mathbf{I}_n$ being an $n \times n$ identity matrix ($I_{ij} = 1$ when $i = j$ and $I_{ij} = 0$ when $i \neq j$) and $\mathscr{K}$ standing for the complex conjugate. Now, solving the characteristic equation

$$\text{Det}(\mathcal{L} - i\omega\mathbf{I}_6) = 0, \tag{4}$$

which yields $\omega^6 + c_1\omega^4 + c_2\omega^2 + c_3 = 0$ with $c_1 = c_3[1 + \eta(2 - \gamma^2 - 2\kappa^2)]$, $c_2 = -c_3(2 - \gamma^2 + \eta)$ and $c_3 = -1/[\eta(1 - 2\kappa^2)]$, one can obtain the corresponding eigenfrequencies. Note that the characteristic equation is a cubic equation with respect to ω^2, thus the six eigenfrequency solutions are the opposite of each other. In what follows, only positive eigenfrequencies are considered for discussion.

For the perturbed PT-symmetric electronic trimer when $\eta \neq 1$, the solution to the characteristic Eq. (4) yields the following set of eigenfrequencies [26], i.e.,

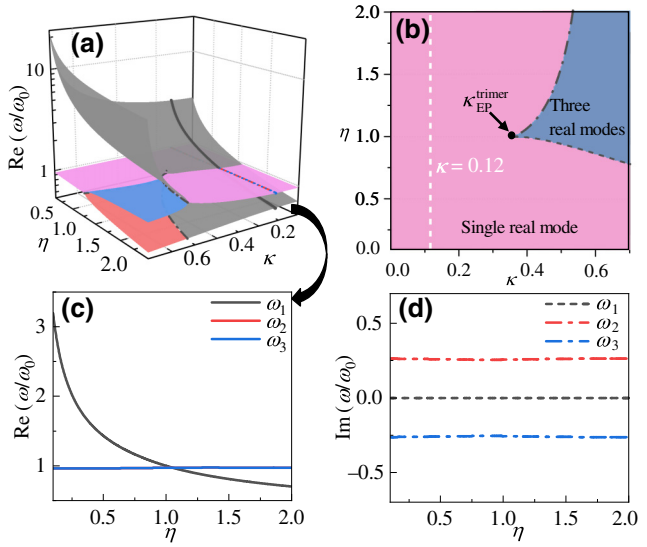

FIG. 2. (a) Real part of system eigenfrequency evolution of perturbed PT-symmetric electronic trimer. (b) The parameter regions for different numbers of real modes in the parameter space (κ, η). (c) Real and (d) imaginary part of eigenfrequency evolution as a function of the perturbation parameter η at $\kappa = 0.12$. Note that, the curves of $\text{Re}(\omega/\omega_0)$ for $\omega_{2,3}$ are overlapped in (c).

$$\omega_{1,4} = \pm\,(s + t - c_1/3)^{1/2}, \tag{5a}$$

$$\omega_{2,5} = \pm\left[-(s+t)/2 + i\sqrt{3}(s-t)/2 - c_1/3\right]^{1/2}, \tag{5b}$$

$$\omega_{3,6} = \pm\left[-(s+t)/2 - i\sqrt{3}(s-t)/2 - c_1/3\right]^{1/2}, \tag{5c}$$

where $s = [p + (p^2 + q^3)^{1/2}]^{1/3}$ and $t = [p - (p^2 + q^3)^{1/2}]^{1/3}$ with $p = -c_1^3/27 + c_1c_2/6 - c_3/2$ and $q = -c_1^2/9 + c_2/3$. Figures 2(a) and 2(b) show the eigenfrequency evolution and the parameter regions for different numbers of real mode at $\gamma = 0.527$ in the parameter space (κ, η). (Here, $\gamma = R\sqrt{C/L}$ with $R = 50\ \Omega$, $C = 100$ pF and $L = 0.9\ \mu$H as used in the experiment verification in Sec. III.) It can be seen that real mode exists in the whole range of (κ, η) of interest for the proposed perturbed non-Hermitian electronic trimer, which indicates that the proposed system is pseudo-Hermitian but not PT symmetric anymore. It is also shown that at different (κ, η), the system can have different numbers of real mode, which is determined by the discriminant $\Delta = p^2 + q^3$. The system exhibits three real modes when $\Delta < 0$ and single real mode when $\Delta > 0$, which are indicated by the blue region and pink region in Fig. 2(b), respectively. Note that three real modes could exist at the same time even though the PT-symmetry condition is not satisfied.

As shown in Fig. 2(b), three real modes can only exist in the strong coupling regime, i.e., $\kappa > \kappa_{\text{EP}}^{\text{trimer}} =$

$\gamma\sqrt{4-\gamma^2}/(2\sqrt{2}) = 0.36$ with $\gamma = R\sqrt{C/L} = 0.527$ as mentioned above, where $\kappa_{\rm EP}^{\rm trimer}$ is approximately a third-order exceptional point of the standard PT-symmetric trimer where three eigenvalues and the corresponding eigenmodes degenerate simultaneously. In the weak coupling regime when $\kappa < \kappa_{\rm EP}^{\rm trimer} = 0.36$, i.e., $\kappa = 0.12$, the system only has one real mode denoted by ω_1 for any given η; and $\omega_{2,3}$ denote a pair of complex conjugate eigenmodes, which can be clearly seen in Figs. 2(c) and 2(d). In this work, the single real mode ω_1 in weak coupling regime, i.e., $\kappa < \kappa_{\rm EP}^{\rm trimer}$, is utilized for the proposed wireless sensing scheme. As for references, we also plot the eigenfrequency evolution as a function of η when $\kappa \geq \kappa_{\rm EP}^{\rm trimer}$ in Appendix B.

It is interesting to notice from Fig. 2(a) that greater eigenfrequency change in response to η occurs with the increase of κ, which yields higher sensitivity. In particular, the divergent EP, $\kappa_D = 1/\sqrt{2}$, observed in the balanced PT-symmetric electronic trimer when $\eta = 1$ has been shown to realize unprecedentedly eigenfrequency bifurcation [23]. However, $1/\sqrt{2}$ is the upper limit of κ for three linearly coupled inductors; and stronger coupling yields shorter interrogation distances, which is not desirable in practical applications. Furthermore, the eigenfrequency is significantly increased as the coupling coefficient κ is increased, which puts forward high requirements for the radio-frequency coils since the inductance of the coil would greatly change due to the eddy current loss at high frequencies. Therefore, we focus on wireless readout only in the weak coupling regime, which enables longer interrogation distances compared with the strong coupling scenarios. Further experimental verification has been carried out to support the proposed readout mechanism in Sec. III.

It should be pointed out that when the perturbation is caused by the loss-side capacitance, the characteristic equation becomes $\omega^6 + c_4\omega^4 + c_2\omega^2 + c_0 + i(c_3\omega^3 + c_1\omega) = 0$, where $c_4 = c_0[1-\kappa^2+\eta(2-\gamma^2-\kappa^2)], c_2 = -c_0[2+(1-\gamma^2)\eta], c_3 = -c_1 = c_0\gamma(1-\eta), c_0 = -1/[\eta(1-2\kappa^2)]$. No explicit eigenfrequency solutions exist and the eigenfrequencies can only be solved numerically, which are six different complex numbers. Thus, the loss side may not function as the sensor, which will break the balanced gain and loss.

III. RESULTS AND DISCUSSIONS

Figure 3 shows the experimental setup of a wireless capacitance readout prototype based on the proposed mechanism. Printed spiral planar inductors with inductance $L = 0.9$ μH are manufactured on three printed circuit boards (PCBs), which are coaxially aligned, i.e., $\Delta x = \Delta y = 0$; and the adjacent vertical distances Δz are adjusted with a positioning stage for coupling parameter tuning (see Appendix D for the detailed information on the coil design). The reflection spectrum S_{11} is measured by connecting the gain resonator to a KEYSIGHT E5063A VNA. Neutral LC tank is used as the sensor whose capacitance C_s can be adjusted from 10 pF to 68 pF so as to respond to the capacitance range corresponding to the physical parameters.

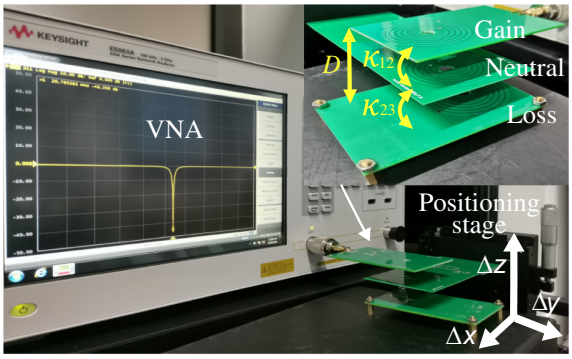

FIG. 3. Experimental setup of the proposed perturbed third-order PT-symmetric wireless sensing system.

Figure 4 plots the reflection spectra of the proposed wireless capacitance readout mechanism when the coupling coefficients between adjacent resonators are $\kappa_{12} = \kappa_{23} = \kappa = 0.12$. Note that in this weak coupling configuration, the coupling between the gain and loss coils κ_{13} can be neglected. Now, the circuit parameters are $L = 0.9$ μH, $R = Z_0 = 50$ Ω and several discrete capacitance values C_s of 10 pF, 22 pF, 30 pF, 47 pF, and 68 pF are chosen to mimic the capacitive sensor. The solid and dashed curves correspond to the experimental and theoretical results of S_{11}, respectively. In our work, the Q factor is defined as the frequency-to-bandwidth ratio of the S_{11} resonance spectra, i.e., $Q = Q_{+3\ \rm dB}^{\rm FWTM} = f_{\rm dip}/\Delta f_{\rm FWTM}^{S_{11}}$, where $f_{\rm dip}$ is the resonant frequency, $\Delta f_{\rm FWTM}^{S_{11}} = f_{\rm dip}^{+} - f_{\rm dip}^{-}$ the bandwidth over which the power is smaller than double the power at the resonant frequency [*namely*, full width at twice minimum (FWTM) akin to FWHM in the field of microwaves and antennas] with $f_{\rm dip}^{\pm}$ denoting the corresponding frequencies when $|S_{11}| = S_{11}^{\rm min} + 3$ dB around $f_{\rm dip}$ ($S_{11}^{\rm min} = |S_{11}|_{f=f_{\rm dip}}$). Since the theoretical $S_{11}^{\rm min}$ can reach several negative hundred in decibels (not shown in Fig. 4, see Fig. 7 for the details), the theoretical $Q_{+3\ \rm dB}^{\rm FWTM}$ factor reads almost infinity, which is much greater than the corresponding experimental $Q_{+3\ \rm dB}^{\rm FWTM}$ factor. It is evident that the frequency $f_{\rm dip}$ corresponding to the sharp dip with great Q factor is shifting as the sensor capacitance C_s is changed, implying the eigenfrequency of the single real mode changes in response to C_s, which validates the aforementioned theoretical analysis. The black solid curve on the (C_s,f) plane illustrates the theoretical eigenfrequency evolution as a function of the sensor capacitance derived from Eq. (5), on which the markers correspond to the experimental dip frequencies of

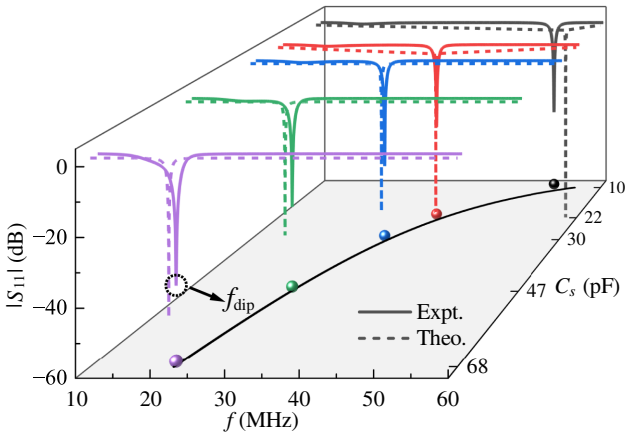

FIG. 4. Theoretical (dashed curves) and experimental (solid curves) of the reflection spectra of the perturbed *PT*-symmetric electronic trimer when the axial separation distance between the gain and loss coils is $D = 30$ mm, which yields the coupling coefficient $\kappa = 0.12$. The black solid curve on the (C_s, f) plane presents the theoretical eigenfrequency evolution as a function of sensor capacitance derived from Eq. (5), and markers on the curve correspond to the measured dip frequency projected from the experimental $|S_{11}|$ curves. The experimental $Q^{\mathrm{FWTM}}_{+3\ \mathrm{dB}}$ factors are 1431, 797, 955, 500, and 505 for C_s of 10 pF, 22 pF, 30 pF, 47 pF, and 68 pF, respectively.

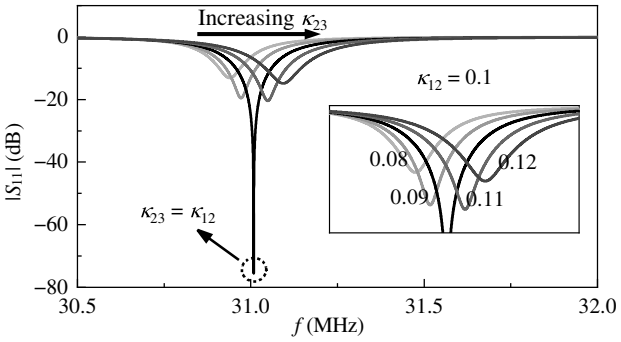

FIG. 5. $|S_{11}|$ spectra for the *PT*-symmetric trimer with asymmetric coupling. When fixing κ_{12} to 0.1 and changing κ_{23} from 0.08 to 0.12, the sharpest curve occurs when κ_{23} is coincident with κ_{12}. The corresponding calculated $Q^{\mathrm{FWTM}}_{+3\ \mathrm{dB}}$ factors read 210, 440, ∞ (almost), 377 and 165, respectively, when κ_{12} varies from 0.08 to 0.12.

each $|S_{11}|$ spectra. We point out that the difference between the experimental and theoretical results will become large when the sensor capacitance is small due to the increase of practical inductance value in high frequency range (see Appendix D for the measured inductance as a function of frequency). Furthermore, the minimum of $|S_{11}|$ can reach -40 dB, which is sufficient enough for capacitance readout. In the experiment, the axial separation distance between the concentric planar spiral inductors on gain and loss side is $D = 30$ mm, yielding the coupling coefficient $\kappa = 0.12$, which indicates that the proposed readout mechanism can provide a high-resolution readout even in weak coupling regime.

For the *PT*-trimer-enhanced wireless readout system, a crucial part is to guarantee balanced coupling coefficient between adjacent inductor coils. In the case of asymmetric coupling when the coupling coefficients of the gain-neutral and neutral-loss coils are not equal, i.e., $\kappa_{12} \neq \kappa_{23}$, the Q factor will degrade significantly even only a slight unbalance of coupling between adjacent coils exhibits. Theoretical results show that when κ_{12} is fixed and as κ_{23} is changed, the reflection spectrum curve with the greatest Q factor corresponds to the case when κ_{23} coincides with κ_{12}, as shown in Fig. 5. Similarly, when κ_{23} is fixed, the sharpest curve occurs when $\kappa_{12} = \kappa_{23}$ as κ_{12} is changed. Therefore, the sharpest curve is found when $\kappa_{12} = \kappa_{23} = \kappa$ in the experiment.

We also compare the performance of the proposed wireless readout mechanism with the conventional method where only a readout antenna and an inductively coupled LC microsensor are incorporated [1], as well as with the standard second-order *PT*-symmetric readout system consisting of inductively coupled RLC resonators with balanced gain and loss, respectively [10], as shown in Fig. 6. Note that we set the coupling coefficient between adjacent inductor coils of *PT*-symmetric trimer to be $\kappa_{\mathrm{trimer}} = 0.2$ while keeping the same interrogation distance for conventional and second-order *PT*-symmetric systems, which yields the corresponding coupling coefficient to be $\kappa_{\mathrm{conv}} = \kappa_{\mathrm{dimer}} = 0.2\sqrt{2}$, as explained in Appendix D. For the conventional readout method, the measured minimum of the reflection spectrum S_{11}^{min} is only greater than about -5 dB [see Fig. 6(a)]. However, for the proposed perturbed third-order *PT*-symmetric wireless readout mechanism, S_{11}^{min} can reach -50 dB, which is ten times larger than that of conventional method, as shown in Fig. 6(c). The proposed readout scheme exhibits greater Q factor compared to the conventional scheme. Therefore, the proposed readout method enables finer spectral resolution in contrast with the conventional method under the same interrogation distance. Compared to standard second-order *PT*-symmetric wireless sensing systems, even though the sensitivity of the proposed third-order *PT*-symmetric system is relatively smaller than the second-order *PT*-symmetric system working in *PT*-symmetric phase nearby the exceptional point (EP), the readout capacitance range is larger. For the second-order *PT*-symmetric system, when the gain (loss) parameter $\gamma = R\sqrt{C/L}$ is less than $\gamma_{\mathrm{EP}} = [2 - 2(1 - \kappa_{\mathrm{dimer}}^2)^{1/2}]^{1/2} = 0.286$ resulting in $C_s < C_{\mathrm{EP}} = L(\gamma_{\mathrm{EP}}/R)^2 = 29.4$ pF, the system is in *PT*-symmetric phase and the readout refection spectrum exhibits greater Q factor, as can be seen from the black and red curves in Fig. 6(b). Particularly, when γ is close to the exceptional point γ_{EP}, the sensitivity can be much higher. Nevertheless, when $\gamma > \gamma_{\mathrm{EP}}$ (i.e., $C_s > C_{\mathrm{EP}}$), the symmetry is

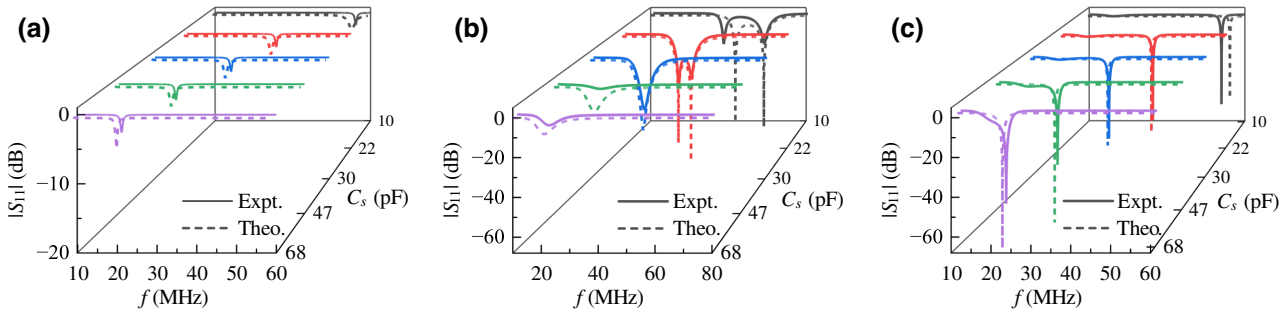

FIG. 6. Comparison of the reflection spectra among (a) conventional, (b) second-order *PT*-symmetric, and (c) the proposed sensing mechanism based on perturbed *PT*-symmetric electronic trimer when $\kappa_{\text{trimer}} = 0.2$ and $\kappa_{\text{conv}} = \kappa_{\text{dimer}} = 0.2\sqrt{2}$. Dashed and solid curves correspond to the theoretical and experimental results, respectively.

spontaneous breaking and the Q factor will degrade significantly as γ is increased, which can be seen from the green and purple curves in Fig. 6(b). Note that in the *PT*-broken phase, the reflection spectrum with high Q factor [see blue curves in Fig. 6(b)] occurs only nearby EP when γ is slightly larger than γ_{EP}, which has been reported in Ref. [35]. Therefore, the readout capacitance range with great Q factor for the second-order *PT*-symmetric system is in the range of $(0, C_{\text{EP}})$. However, for the proposed third-order *PT*-symmetric system, the readout capacitance range is $(0, C_{\text{max}})$ where C_{max} can be set arbitrarily according to the specific application scenario to cover the whole quantity to be measured. In our experiment, the capacitance of gain (loss) resonators is chosen as $C = 100$ pF, therefore the readout capacitance range is $(0, 100$ pF), while for second-order *PT*-based system the corresponding range will be $(0, 29.4$ pF). The experimental Q factors correspond to Fig. 6 are summarized in Table I. Note that the measured spectra resonances for the conventional scheme are so weak that $Q^{\text{FWTM}}_{+3\text{ dB}}$ factors are no longer applicable.

Figure 7 compares the theoretical reflection coefficient minimums S_{11}^{min} of the proposed perturbed third-order *PT*-symmetric wireless readout mechanism with the conventional and the standard second-order *PT*-symmetric readout system by substituting the analytical eigenfrequencies of each case into the reflection coefficient [see Eq. (C3) in Appendix C]. For the conventional second-order *PT*-symmetric case, two eigenfrequencies are considered, respectively, which are two real numbers in the *PT*-symmetric phase when $\kappa > \kappa_{\text{EP}}^{\text{dimer}}$ and a pair of complex conjugate numbers in the *PT*-broken phase when $\kappa < \kappa_{\text{EP}}^{\text{dimer}}$. Here, the range of the coupling coefficient κ is $(0, 0.45)$ for comparison in weak coupling regime; the sensor capacitance is fixed to $C_s = 30$ pF; and the sensor resistance of conventional system is $R = 0.5\ \Omega$. Note that for standard second-order *PT*-based systems, it requires the reader capacitance $C_r = C_s = 30$ pF, $L = 0.9\ \mu$H, and sensor resistance $R = Z_0 = 50\ \Omega$ yielding the corresponding gain (loss) parameter $\gamma = 0.289$. Comparing the blue solid lines and discrete black data points in Fig. 7, it is evident that the proposed perturbed third-order *PT*-symmetric readout mechanism exhibits much greater S_{11}^{min} than the conventional method where high Q factor exists only in a limited range of κ. Compared to the standard second-order *PT*-based system, the S_{11}^{min} of the proposed system can maintain large absolute value (high Q-factor) in the whole range of κ. However, for the conventional second-order *PT*-based system, high Q factor exists only in the *PT*-symmetric phase when $\kappa > \kappa_{\text{EP}}^{\text{dimer}} = \gamma\sqrt{1-\gamma^2/4} = 0.286$ and in the *PT*-broken phase nearby EP [35], but will degrade significantly as κ becomes small. Therefore, the proposed perturbed third-order *PT*-symmetric readout mechanism shows better performance in the weak coupling regime compared to the standard second-order *PT*-symmetric system. Furthermore, the minimum S_{11} of the proposed system is decreasing as the coupling coefficient κ is increased, implying deeper spectrum dip, which is originated from the stronger reflected waves from neutral and loss resonators. Note that even though the minimum S_{11} can reach about -700 dB for the proposed third-order and the standard second-order *PT*-based system in *PT*-symmetric phase in theory, practical measured spectrum can reach only several tens of decibels due to the limited sweep point, which may skip the lowest dip.

The inset of Fig. 7 shows the theoretical reflection spectra evolution of the proposed readout mechanism as κ increases from 0.05 to 0.2. It can be seen that both the dip frequency f_{dip} and S_{11}^{min} are dependent on the coupling

TABLE I. Comparison of the $Q^{\text{FWTM}}_{+3\text{ dB}}$ factors between the second-order *PT*-symmetric dimer (*PT* dimer) and the proposed perturbed *PT*-symmetric trimer (perturbed trimer), corresponding to Figs. 6(b) and 6(c), respectively.

C_s	10 pF	22 pF	30 pF	47 pF	68 pF
$Q_{PT\text{ dimer}}$	47.65[a]	47.1[a]	27.1	[b]	
$Q_{\text{Perturbed trimer}}$	226.10	162.23	178.69	130.45	62.66

[a]Resonances at higher frequency are measured.
[b]Not applicable since $S_{11}^{\text{min}} > -3$ dB.

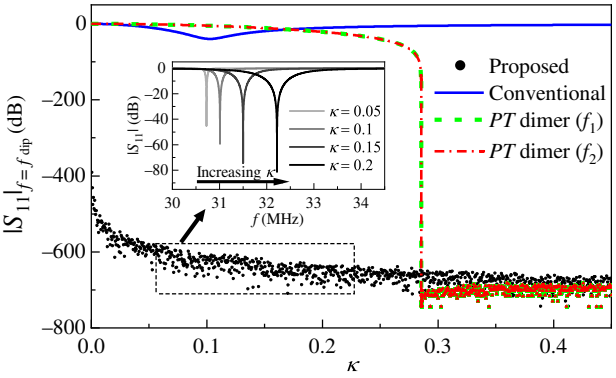

FIG. 7. Minimum of $|S_{11}|$ comparison between conventional, standard *PT*-symmetric dimer and the proposed perturbed *PT*-symmetric electronic trimer when $C_s = 30$ pF (In the standard *PT*-symmetric dimer, $C_r = C_s = 30$ pF, which yields gain (loss) parameter $\gamma = 0.289$). The inset illustrates the reflection spectrum of the proposed perturbed third-order *PT*-symmetric readout mechanism with different coupling coefficient. The dip frequencies correspond to $\kappa = 0.05$, 0.10, 0.15, and 0.20 are 30.73, 31.01, 31.5, and 32.22 MHz, respectively; and the -3 dB bandwidth reads 0.077, 0.311, 0.706, and 1.274 MHz, respectively.

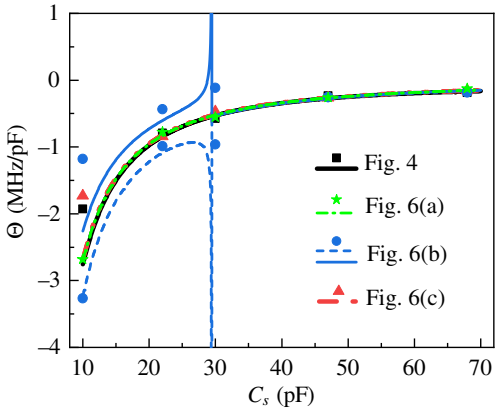

FIG. 8. Theoretical (curves) and experimental (markers) sensitivity Θ as a function of the sensor capacitance C_s of the proposed readout method at $\kappa = 0.2$ [Fig. 6(c), red] and $\kappa = 0.12$ (Fig. 4, black), in comparison with the corresponding sensitivities of conventional [Fig. 6(a), green] and *PT*-dimer-based readout method at $\kappa = 0.2\sqrt{2}$ [Fig. 6(b), blue].

coefficient κ. Specifically, $S_{11}^{\min}$ becomes smaller and the resonance line width (-3 dB) becomes broader as κ is increased. Moreover, the dip frequency f_{dip} is approaching to the natural resonance frequency of the sensor resonator, i.e., $f_s = 30.63$ MHz, as κ is decreased. It should be pointed out that even though the position of the $|S_{11}|$ minimum is higher in the weak coupling regime, the line width is narrower implying higher spectral resolution, which validates the feasibility of the proposed *PT*-symmetric-trimer-based sensing mechanism in application scenarios where longer interrogation distances are required.

Finally, we discuss the sensitivity of the proposed perturbed *PT*-symmetric trimer, which is defined as $\Theta = \partial f_{\text{dip}}/\partial C_s$. The dip frequency $f_{\text{dip}} = (2\pi)^{-1}\omega_0\omega_1$, with $\omega_0 = 1/\sqrt{LC}$ being the natural resonance frequency of gain (loss) *LC* resonator and ω_1 given in Eq. (5), is as a function of the sensor capacitance $C_s = \eta C$ for a fixed κ. By fitting the experimental data with B-spline function, experimental sensitivities are approximated with the first derivative of the fitting curve at each C_s point. Figure 8 presents the theoretical and experimental sensitivity Θ as a function of the sensor capacitance C_s of the proposed readout method at $\kappa = 0.2$ (black curve and markers) and $\kappa = 0.12$ (red curve and markers), respectively. It can be seen that the absolute value $|\Theta|$ is deceasing as C_s is increased. Specifically, the calculated sensitivities increases from -1.93 MHz/pF to -0.19 MHz/pF as C_s varies from 10 to 68 pF. Moreover, the consistency of the black curve and the red curve implies that the sensitivity is independent of the coupling coefficient κ in weak coupling regime. We also compare the sensitivity of the proposed system with that of conventional (green curve and markers) and *PT*-dimer-based (blue curves and markers; blue solid line and dashed line, respectively, corresponds to the sensitivity of higher-frequency and lower-frequency branch dip shift in Fig. 6) readout method at $\kappa = 0.2\sqrt{2}$. In addition, the sensitivity of the proposed system is comparable to conventional method and *PT*-dimer-based sensing system in symmetry-broken phase. Furthermore, the *PT*-dimer-based readout system exhibits higher sensitivity for the high-frequency branch when functioning in *PT*-symmetric phase and can reach ∞ in theory as C_s approaches C_{EP}. Enhanced sensitivity at the exceptional point is also an intriguing feature of *PT*-symmetric systems and has been extensively studied [37], which is not discussed in detail in this paper.

IV. CONCLUSION

In summary, we report a sandwich-type wireless capacitance readout system based on parity-time-symmetric electronic trimer consisting of a gain-neutral-loss *LC* resonator chain. Theoretical analysis and experimental verification show that perturbing the neutral resonator of the trimer can realize wireless capacitance readout with high Q factor thanks to the existence of a single real mode of the system in the weak coupling regime. Compared to conventional wireless sensing systems, the proposed mechanism exhibits finer spectral resolution due to the higher Q factor. Different from the standard second-order [10] and third-order [23] *PT*-symmetric systems, the proposed readout mechanism functions in the weak coupling regime, extending the interrogation distance between sensor and reader tank while maintaining ultrahigh resolution. Furthermore,

the capacitors on gain and loss side do not need to be manually tuned to maintain the *PT* symmetry condition and the readout capacitance range is wider whose upper bound is determined by the capacitance of gain (loss) *LC* tank. Thus, the proposed wireless sensing method is more suitable for application scenarios, such as implanted medical devices where longer interrogation distance is usually required, providing a practical pathway toward the *PT*-enhanced wireless sensing.

ACKNOWLEDGMENT

T.D. acknowledges support from National Natural Science Foundation of China (NSFC) under Grant No. 51977165.

APPENDIX A: DERIVATION OF SYSTEM EQUATIONS FOR *PT*-SYMMETRIC ELECTRONIC TRIMER

Applying Kirchhoff's laws to the *PT*-symmetric trimer circuit shown in Fig. 1(b), one can obtain the following system equations as

$$-I_1 Z_0 + V_{C_1} + V_{L1} = 0, \tag{A1a}$$

$$V_{C_2} + V_{L_2} = 0, \tag{A1b}$$

$$I_3 R + V_{C_3} + V_{L3} = 0, \tag{A1c}$$

where V_{C_n} for $n = 1, 2, 3$ represent the capacitor voltage of series gain, neutral and loss resonators, respectively; the $i - v$ relation of the inductors yields $V_{L1} = LI_1'(t) + MI_2'(t)$, $V_{L2} = LI_2'(t) + M[I_1'(t) + I_3'(t)]$ and $V_{L3} = LI_3'(t) + MI_2'(t)$; $I_n(t) = C_n V_{C_n}'(t)$ stands for each inductor current; $I_n'(t)$ [or $V_{C_n}'(t)$] denotes the first-order derivatives of $I_n(t)$ [or $V_{C_n}(t)$] with respect to the variable t. By defining the coupling coefficient $\kappa = L/M$, gain (loss) parameter $\gamma = R\sqrt{C/L} = Z_0\sqrt{C/L}$, natural resonance frequency $\omega_0 = 1/\sqrt{LC}$ and the normalized time (phase) $\tau = \omega_0 t$, the second-order ordinary differential system equations can be derived as

$$I_1''(\tau) = -\frac{1-\kappa^2}{1-2\kappa^2} I_1 + \frac{1}{\eta}\frac{\kappa}{1-2\kappa^2} I_2 - \frac{\kappa^2}{1-2\kappa^2} I_3 + \gamma\frac{1-\kappa^2}{1-2\kappa^2} I_1'(\tau) - \gamma\frac{\kappa^2}{1-2\kappa^2} I_3'(\tau), \tag{A2a}$$

$$I_2''(\tau) = -\frac{1}{\eta(1-2\kappa^2)} I_2 + \frac{\kappa}{1-2\kappa^2}(I_1 + I_3) - \gamma\frac{\kappa}{1-2\kappa^2} I_1'(\tau) + \gamma\frac{\kappa}{1-2\kappa^2} I_3'(\tau), \tag{A2b}$$

$$I_3''(\tau) = -\frac{1-\kappa^2}{1-2\kappa^2} I_3 + \frac{1}{\eta}\frac{\kappa}{1-2\kappa^2} I_2 - \frac{\kappa^2}{1-2\kappa^2} I_1 + \gamma\frac{\kappa^2}{1-2\kappa^2} I_1'(\tau) - \gamma\frac{1-\kappa^2}{1-2\kappa^2} I_3'(\tau), \tag{A2c}$$

which are three coupled second-order differential equations. Here, the primes and double primes denote the first- and second-order derivatives with respect to the normalized time τ, respectively. By considering an $\exp(i\omega\tau)$ time dependence and defining the state vector as $\Phi = (I_1, I_2, I_3, I_1', I_2', I_3')^T$, the system equations can be recast into the Liouvillian formalism as given by Eqs. (1) and (2) in the main text.

APPENDIX B: EIGENFREQUENCY EVOLUTION OF PERTURBED *PT* ELECTRONIC TRIMER AT EXCEPTIONAL POINT AND IN STRONG COUPLING REGIME

The proposed readout mechanism may be functional even when κ is large in theory. Figures 9(a) and 9(c) plot the eigenfrequency evolution as a function of the perturbation parameter η when the coupling coefficient κ reads 0.36 and 0.7, respectively. When $\kappa = \kappa_{\mathrm{EP}}^{\mathrm{trimer}} = \gamma\sqrt{4-\gamma^2}/(2\sqrt{2}) = 0.36$, three real eigenfrequencies exhibit at the same time only when $\eta = 1$ where the three modes coalesce and become a third-order degeneracy. In addition, the system exhibits only one real mode denoted by ω_1 and a pair of complex conjugate modes denoted by $\omega_{2,3}$. In the strong coupling regime, such as $\kappa = 0.7$, the eigenfrequency evolution with respect to η exhibits two regions: when $\eta < 0.782$, the system has one real eigenvalue ω_1 and a pair of conjugate eigenvalues $\omega_{2,3}$; when $\eta > 0.782$, the system exhibits three real eigenvalues. The second-order exceptional point $\eta = 0.782$ is where ω_2 and ω_3 coalesce and become a second-order degeneracy. It should be noted that the real eigenfrequency ω_1 exhibits a dramatic change in response to η when κ is close to $\sqrt{2}/2$, which is the upper limit of three linearly coupled inductors.

Figures 9(b) and 9(d) illustrate the readout reflection spectra evolution with respect to η when κ reads 0.36 and 0.7, respectively. When $\kappa = 0.36$ at the exceptional point, three dips are observed at $\eta = 1$ due to the degeneracy of the eigenfrequency; and only one dip appears when $\eta \neq 1$. When $\kappa = 0.7$ in the strong coupling regime, a significant dip frequency shift is observed for the high-frequency branch corresponding to ω_1, as shown in Fig. 9(c), which indicates high sensitivity. As for the low-frequency branches corresponding to $\omega_{2,3}$ when $\eta > 1$, such a system may also be functional. However, as discussed in the main text, the larger coupling coefficient κ, the shorter interrogation distance will be. Moreover, it can be very difficult to realize the required inductor when κ is large for practical wireless sensing applications. Therefore, despite that the proposed readout mechanism seems functional when κ is large in theory, it would actually fail in practice since the operating frequency is large, e.g., several hundred MHz when $\kappa = 0.7$, as shown in 9(d). Similar to the weak coupling scenario when $\kappa = 0.12$, the

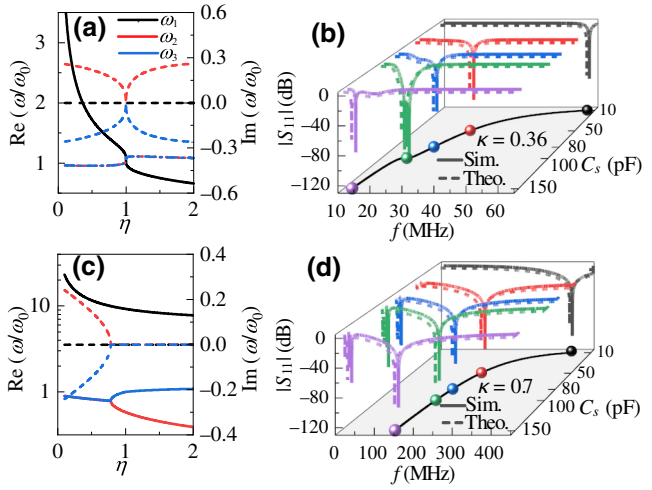

FIG. 9. Real (solid curves) and imaginary (dashed curves) part of eigenfrequency evolution as a function of the perturbation parameter η when the coupling coefficients reads (a) $\kappa = 0.36$ and (c) $\kappa = 0.7$. Here, black, red, and blue curves correspond to ω_1, ω_2, and ω_3, respectively. Note that, the curves of $\mathrm{Re}(\omega/\omega_0)$ for $\omega_{2,3}$ are overlapped in (a). Simulated (solid curves) and theoretical (dashed curves) readout reflection spectra evolution in response to η when (b) $\kappa = 0.36$ and (d) $\kappa = 0.7$. The black solid curve and markers on the (C_s, f) plane present the theoretical eigenfrequency ω_1 evolution as a function of sensor capacitance.

theoretical Q factors reach almost infinity when $\kappa = 0.36$ and $\kappa = 0.7$. Also, the theoretical sensitivity characteristics behave the same as those for $\kappa = 0.1$ and $\kappa = 0.2$, as shown in Fig. 8.

APPENDIX C: DERIVATION OF THE REFLECTION COEFFICIENTS FOR CONVENTIONAL *LC* SENSORS, STANDARD *PT*-SYMMETRIC DIMERS AND THE PROPOSED PERTURBED *PT*-SYMMETRIC TRIMERS

For the sinusoidal steady-state circuit of the proposed wireless capacitance readout system shown in Fig. 1(b), according to Kirchhoff's law, one can obtain

$$i(\omega - \omega^{-1})I_3 + \gamma I_3 + i\omega\kappa I_2 = 0, \tag{C1a}$$

$$i(\omega - \eta^{-1}\omega^{-1})I_2 + i\omega\kappa(I_1 + I_3) = 0, \tag{C1b}$$

$$i(\omega - \omega^{-1})I_1 + i\omega\kappa I_2 = \gamma V_{\mathrm{in}}/R. \tag{C1c}$$

Here, ω is normalized by the natural resonance frequency $\omega_0 = 1/\sqrt{LC}$; $\gamma = R\sqrt{C/L}$ is the normalized gain (loss) parameter; $\kappa = M/L$ is the coupling coefficient; and $\eta = C_s/C$ is the capacitive perturbation parameter. By evaluating for $Z_{\mathrm{in}} = V_{\mathrm{in}}/I_1$, the input impedance of the perturbed *PT*-symmetric trimer can be derived as

$$Z_{\mathrm{in}}^{\mathrm{trimer}} = R\frac{(1-\omega^2)[h(\omega) - \eta\kappa^2\omega^4] + i\gamma\omega h(\omega)}{\gamma\omega[\gamma\omega(\eta\omega^2 - 1) + ih(\omega)]}, \tag{C2}$$

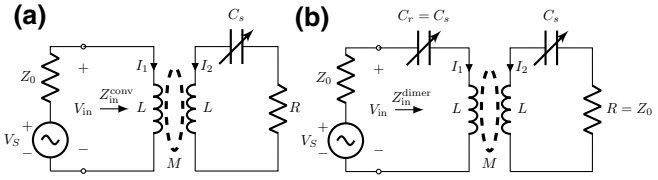

FIG. 10. (a) Conventional *LC* wireless sensor readout mechanism and (b) *PT*-symmetric *LC* wireless sensor with second-order EP.

where $h(\omega) = \eta(1-\kappa^2)\omega^4 - (1+\eta)\omega^2 + 1$. Consequently, the reflection coefficient can then be calculated as

$$S_{11} = 20\lg\left|\frac{Z_{\mathrm{in}} - Z_0}{Z_{\mathrm{in}} + Z_0}\right|, \tag{C3}$$

where $Z_0 = 50\ \Omega$ is the intrinsic impedance of the VNA.

As a reference, Fig. 10(a) illustrates the schematic circuit for a conventional *LC* wireless readout system, where the sensor coil together with a capacitive sensor is inductively coupled to the readout coil.

The value of the capacitive sensor is measured through the dip shift of the reflection spectrum. Now, Kirchhoff's law yields $i(\omega - \omega^{-1})I_2 + \gamma I_2 + i\omega\kappa I_1 = 0$ and $V_{\mathrm{in}}\gamma/R = i\omega I_1 + i\omega\kappa I_2$; thus, the input impedance $Z_{\mathrm{in}} = V_{\mathrm{in}}/I_1$ can be expressed as

$$Z_{\mathrm{in}}^{\mathrm{conv}} = R\frac{\omega[i\gamma\omega - (1-\kappa^2)\omega^2 + 1]}{\gamma[\gamma\omega - i(1-\omega^2)]}. \tag{C4}$$

For the *PT*-symmetric sensor with second-order EP, whose schematic circuit is shown in Fig. 10(b), the reader circuit is replaced by a *RLC* series resonator with negative resistance. Kirchhoff's law yields $i(\omega - \omega^{-1})I_2 + \gamma I_2 + i\omega\kappa I_1 = 0$ and $V_{\mathrm{in}}\gamma/R = i(\omega - \omega^{-1})I_1 + i\omega\kappa I_2$; and the input impedance $Z_{\mathrm{in}} = V_{\mathrm{in}}/I_1$ now reads as

$$Z_{\mathrm{in}}^{\mathrm{dimer}} = R\frac{i\gamma(\omega^2 - 1)\omega - (1-\kappa^2)\omega^4 + 2\omega^2 - 1}{\gamma\omega[\gamma\omega - i(1-\omega^2)]}. \tag{C5}$$

When R, Z_0, L, γ, and κ are known, the theoretical frequency response of the reflection coefficient S_{11} defined in Eq. (C3) can be obtained, as demonstrated in Fig. 6 of the main text.

APPENDIX D: COIL DESIGN, RELATION BETWEEN THE COUPLING COEFFICIENTS OF CONCENTRICALLY ALIGNED COIL DIMERS AND TRIMERS

In order to validate the proposed readout mechanism in radio-frequency range, we design a planar spiral inductor on board, as illustrated in Fig. 11(a). The self-inductance

of printed spiral coils is obtained from the ratio of the magnetic flux generated by the conductor to the current, which can be approximated by the closed form as [38]

$$L \approx 0.5\mu_0 N^2 \phi_{\text{avg}} \left(0.9 + 0.2f^2 - \ln f\right), \tag{D1}$$

where μ_0 is the vacuum permeability; $\phi_{\text{avg}} = 2r_{\text{in}} + N(w+s)$ is the average diameter of the coil with r_{in} denoting inner radius, w and s being the width and spacing of the spiral coil, respectively, and N being the number of turns; $f = (r_{\text{out}} + r_{\text{in}})/(r_{\text{out}} - r_{\text{in}})$ is filling rate with r_{out} being the outer radius of the coil.

Due to the existence of parasitic capacitance affected by coil size, the inductance would increase with frequency. To realize the frequency-stable and almost nondispersive target inductance of $L = 0.9$ μH at a frequency range from 10 to 60 MHz, the geometric parameters of the coils reads as $N = 5.05$, $r_{\text{in}} = 8$ mm, and $s = w = 1.188$ mm. Figure 11(b) shows the simulated and measured inductance of the designed coils as a function of frequency, which further validates our design scheme. We also carry out full-wave simulation in order to evaluate the mutual inductance M between two coaxial coils, and further obtain the coupling coefficient $\kappa = M/L$, as illustrated in Fig. 11(c). It can be seen that the coupling coefficient is decreased as the distance between coaxial coils is increased. In the weak coupling region when the separation distance d is large, the coupling coefficient is almost frequency stable.

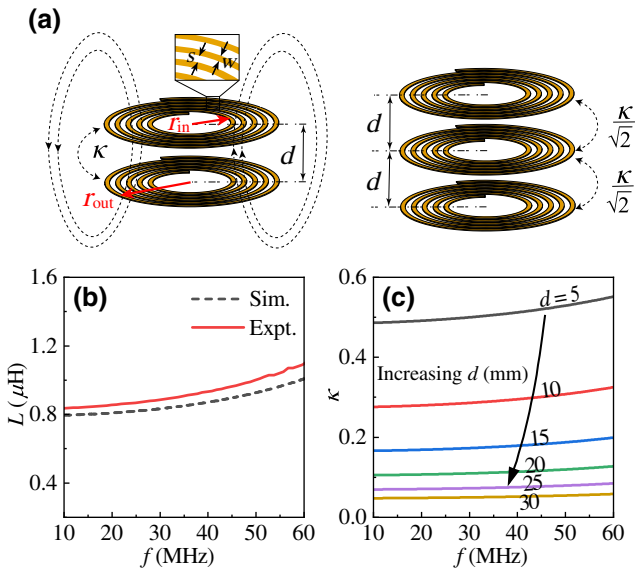

FIG. 11. (a) Illustration of concentrically aligned printed spiral coil dimer (left) and trimer (right). When the separations distance of two adjacent coils are equal, the coupling coefficient of the trimer is that of dimer divided by $\sqrt{2}$. (b) Measured (solid curves) and simulated (dashed curves) self-inductance of the designed coils. (c) The coupling coefficients under different working frequencies for various separation distance.

It should also be pointed out that for the same interrogation distance, the coupling coefficient between two concentric coils and adjacent coupling of three concentric coils is different. Assuming the inductances of the three coils in Fig. 11(a) are $L_1 = L_2 = L_3 = L$ ("1" for the gain, "2" for the neutral LC tank, and "3" for the loss), and the mutual inductances between adjacent coils are $M_{12} = M_{23} = M$. Thus, the energy stored in the inductors reads $W = L(I_1^2 + I_2^2 + I_3^2)/2 + MI_1I_2 + MI_2I_3$, which can be expressed in the matrix form as $W = \frac{1}{2}I^T\mathcal{M}I$, where

$$\mathcal{M} = \begin{pmatrix} L & M & 0 \\ M & L & M \\ 0 & M & L \end{pmatrix} \tag{D2}$$

is the mutual inductance matrix and $I = (I_1, I_2, I_3)^T$. Due to the arbitrariness of the current, the inductance matrix must be positive definite to guarantee that the energy is positive, which yields $L^3 - 2LM^2 > 0$. Therefore, for the concentrically aligned coil trimer, $\kappa = M/L < \sqrt{2}/2$. As a result, if the coupling coefficient reads κ for the coil dimer when the separation distance is d, the coupling coefficient becomes $\kappa/\sqrt{2}$ for the concentric coil trimer with the same adjacent separation distances.

[1] P.-J. Chen, S. Saati, R. Varma, M. S. Humayun, and Y.-C. Tai, Wireless intraocular pressure sensing using microfabricated minimally invasive flexible-coiled LC sensor implant, J. Microelectromech. Syst. **19**, 721 (2010).

[2] C. M. Boutry, L. Beker, Y. Kaizawa, C. Vassos, H. Tran, A. C. Hinckley, R. Pfattner, S. Niu, J. Li, J. Claverie, *et al.*, Biodegradable and flexible arterial-pulse sensor for the wireless monitoring of blood flow, Nat. Biomed. Eng. **3**, 47 (2019).

[3] W.-J. Deng, L.-F. Wang, L. Dong, and Q.-A. Huang, LC wireless sensitive pressure sensors with microstructured PDMS dielectric layers for wound monitoring, IEEE Sens. J. **18**, 4886 (2018).

[4] J. E. Rogers, Y.-K. Yoon, M. Sheplak, and J. W. Judy, A passive wireless microelectromechanical pressure sensor for harsh environments, J. Microelectromech. Syst. **27**, 73 (2017).

[5] Y. Ji, Q. Tan, H. Wang, W. Lv, H. Dong, and J. Xiong, A novel surface LC wireless passive temperature sensor applied in ultra-high temperature measurement, IEEE Sens. J. **19**, 105 (2018).

[6] M. H. Zarifi and M. Daneshmand, High-resolution RFID liquid sensing using a chipless tag, IEEE Microw. Wirel. Compon. Lett. **27**, 311 (2017).

[7] R. Nopper, R. Niekrawietz, and L. Reindl, Wireless readout of passive LC sensors, IEEE Trans. Instrum. Meas. **59**, 2450 (2009).

[8] Z. Xu, Y. Wang, J. Chang, and T. J. Cui, Multiple Spoof Plasmonically Induced Transparency for Sensing Applications, Phys. Rev. Appl. **18**, 024035 (2022).

[9] J. Streque, J. Camus, T. Laroche, S. Hage-Ali, H. M'Jahed, M. Rammal, T. Aubert, M. A. Djouadi, S. Ballandras, and O. Elmazria, Design and characterization of high-Q SAW resonators based on the AlN/sapphire structure intended for high-temperature wireless sensor applications, IEEE Sens. J. **20**, 6985 (2020).

[10] P.-Y. Chen, M. Sakhdari, M. Hajizadegan, Q. Cui, M. M.-C. Cheng, R. El-Ganainy, and A. Alù, Generalized parity-time symmetry condition for enhanced sensor telemetry, Nat. Electron. **1**, 297 (2018).

[11] C. M. Bender and S. Boettcher, Real Spectra in Non-Hermitian Hamiltonians Having $\mathcal{PT}$ Symmetry, Phys. Rev. Lett. **80**, 5243 (1998).

[12] A. Guo, G. J. Salamo, D. Duchesne, R. Morandotti, M. Volatier-Ravat, V. Aimez, G. A. Siviloglou, and D. N. Christodoulides, Observation of $\mathcal{PT}$-Symmetry Breaking in Complex Optical Potentials, Phys. Rev. Lett. **103**, 093902 (2009).

[13] C. E. Rüter, K. G. Makris, R. El-Ganainy, D. N. Christodoulides, M. Segev, and D. Kip, Observation of parity-time symmetry in optics, Nat. Phys. **6**, 192 (2010).

[14] Ş. K. Özdemir, S. Rotter, F. Nori, and L. Yang, Parity-time symmetry and exceptional points in photonics, Nat. Mater. **18**, 783 (2019).

[15] J. Schindler, A. Li, M. C. Zheng, F. M. Ellis, and T. Kottos, Experimental study of active LRC circuits with PT symmetries, Phys. Rev. A **84**, 040101(R) (2011).

[16] J. Schindler, Z. Lin, J. Lee, H. Ramezani, F. M. Ellis, and T. Kottos, PT-symmetric electronics, J. Phys. A: Math. Theor. **45**, 444029 (2012).

[17] S. Assawaworrarit, X. Yu, and S. Fan, Robust wireless power transfer using a nonlinear parity-time-symmetric circuit, Nature **546**, 387 (2017).

[18] J. Zhou, B. Zhang, W. Xiao, D. Qiu, and Y. Chen, Nonlinear parity-time-symmetric model for constant efficiency wireless power transfer: Application to a drone-in-flight wireless charging platform, IEEE Trans. Ind. Electron. **66**, 4097 (2018).

[19] C. Zeng, Y. Sun, G. Li, Y. Li, H. Jiang, Y. Yang, and H. Chen, High-Order Parity-Time Symmetric Model for Stable Three-Coil Wireless Power Transfer, Phys. Rev. Appl. **13**, 034054 (2020).

[20] S. Assawaworrarit and S. Fan, Robust and efficient wireless power transfer using a switch-mode implementation of a nonlinear parity-time symmetric circuit, Nat. Electron. **3**, 273 (2020).

[21] Z. Xiao, H. Li, T. Kottos, and A. Alù, Enhanced Sensing and Nondegraded Thermal Noise Performance Based on PT-Symmetric Electronic Circuits with a Sixth-Order Exceptional Point, Phys. Rev. Lett. **123**, 213901 (2019).

[22] Z. Dong, Z. Li, F. Yang, C.-W. Qiu, and J. S. Ho, Sensitive readout of implantable microsensors using a wireless system locked to an exceptional point, Nat. Electron. **2**, 335 (2019).

[23] M. Sakhdari, M. Hajizadegan, Q. Zhong, D. N. Christodoulides, R. El-Ganainy, and P.-Y. Chen, Experimental Observation of PT Symmetry Breaking Near Divergent Exceptional Points, Phys. Rev. Lett. **123**, 193901 (2019).

[24] M. Yang, Z. Ye, M. Farhat, and P.-Y. Chen, Ultrarobust wireless interrogation for sensors and transducers: A non-Hermitian telemetry technique, IEEE Trans. Instrum. Meas. **70**, 1 (2021).

[25] M. Yang, Z. Ye, N. Alsaab, M. Farhat, and P.-Y. Chen, In-vitro demonstration of ultra-reliable, wireless and batteryless implanted intracranial sensors operated on loci of exceptional points, IEEE Trans. Biomed. Circuits Syst. **16**, 287 (2022).

[26] K. Yin, Y. Huang, C. Ma, X. Hao, X. Gao, X. Ma, and T. Dong, Wireless real-time capacitance readout based on perturbed nonlinear parity-time symmetry, Appl. Phys. Lett. **120**, 194101 (2022).

[27] S. Bittner, B. Dietz, U. Günther, H. L. Harney, M. Miski-Oglu, A. Richter, and F. Schäfer, PT Symmetry and Spontaneous Symmetry Breaking in a Microwave Billiard, Phys. Rev. Lett. **108**, 024101 (2012).

[28] Z. Fan, W. Zhang, Q. Qiu, and J. Yao, Hybrid frequency-tunable parity-time symmetric optoelectronic oscillator, J. Lightwave Technol. **38**, 2127 (2020).

[29] R. Fleury, D. Sounas, and A. Alù, An invisible acoustic sensor based on parity-time symmetry, Nat. Commun. **6**, 1 (2015).

[30] R. Fleury, D. L. Sounas, and A. Alù, Parity-time symmetry in acoustics: Theory, devices, and potential applications, IEEE J. Sel. Top. Quantum Electron. **22**, 121 (2016).

[31] Y. Yang, H. Jia, Y. Bi, H. Zhao, and J. Yang, Experimental Demonstration of an Acoustic Asymmetric Diffraction Grating Based on Passive Parity-Time-Symmetric Medium, Phys. Rev. Appl. **12**, 034040 (2019).

[32] X. Hao, J. Zou, K. Yin, X. Ma, and T. Dong, Enhanced power conversion capability of class-E power amplifiers with GaN HEMT based on cross-quadrant operation, IEEE Trans. Power Electron. **37**, 13966 (2022).

[33] X. Hao, J. Zou, R. Wang, K. Yin, Y. Huang, X. Ma, and T. Dong, Frequency-stable robust wireless power transfer based on high-order pseudo-Hermitian physics, arXiv:2208.00633 (2022).

[34] S. Kananian, G. Alexopoulos, and A. S. Y. Poon, Coupling-Independent Real-Time Wireless Resistive Sensing Through Nonlinear $\mathcal{PT}$ Symmetry, Phys. Rev. Appl. **14**, 064072 (2020).

[35] B.-B. Zhou, W.-J. Deng, L.-F. Wang, L. Dong, and Q.-A. Huang, Enhancing the Remote Distance of *LC* Passive Wireless Sensors by Parity-Time Symmetry Breaking, Phys. Rev. Appl. **13**, 064022 (2020).

[36] B.-B. Zhou, L.-F. Wang, L. Dong, and Q.-A. Huang, Observation of the perturbed eigenvalues of PT-symmetric LC resonator systems, J. Phys. Commun. **5**, 045010 (2021).

[37] H. Hodaei, A. U. Hassan, S. Wittek, H. Garcia-Gracia, R. El-Ganainy, D. N. Christodoulides, and M. Khajavikhan, Enhanced sensitivity at higher-order exceptional points, Nature **548**, 187 (2017).

[38] S. S. Mohan, M. del Mar Hershenson, S. P. Boyd, and T. H. Lee, Simple accurate expressions for planar spiral inductances, IEEE J. Solid-State Circuits **34**, 1419 (1999).